JGR Space Physics

RESEARCH ARTICLE
10.1029/2022JA031252

Key Points:

- Enhancement of field-aligned warm ions observed in the plasma sheet was energy-dispersive with increasing energy from 20 eV to >100 eV
- The probe at larger r observed the energy-dispersive enhancements 20 min earlier than did the probe at smaller r
- The enhancements were likely caused by enhanced convection and the dispersion was likely due to acceleration by field-aligned potential

Correspondence to:
C.-P. Wang,
cat@atmos.ucla.edu

Citation:
Wang, C.-P., Wang, X., Lin, Y., Wing, S., & Hairston, M. (2023). Energy-dispersive field-aligned warm ion enhancement in the plasma sheet during a substorm growth phase: A THEMIS event. *Journal of Geophysical Research: Space Physics*, *128*, e2022JA031252. https://doi.org/10.1029/2022JA031252

Received 20 DEC 2022
Accepted 13 MAY 2023

Energy-Dispersive Field-Aligned Warm Ion Enhancement in the Plasma Sheet During a Substorm Growth Phase: A THEMIS Event

Chih-Ping Wang[1], Xueyi Wang[2], Yu Lin[2], Simon Wing[3], and Marc Hairston[4]

[1]Department of Atmospheric and Oceanic Sciences, University of California, Los Angeles, Los Angeles, CA, USA, [2]Physics Department, Auburn University, Auburn, AL, USA, [3]The Johns Hopkins University Applied Physics Laboratory, Laurel, MD, USA, [4]William B. Hanson Center for Space Sciences, University of Texas at Dallas, Richardson, TX, USA

Abstract We present an event of field-aligned warm (10–1,000 eV) ion enhancement with an energy-dispersion signature with increasing energy that has never been reported before and propose that such dispersion was a result of outflow ions being gradually accelerated by intensifying upward field-aligned potential. The energy-dispersive enhancement with increasing energy from ~20 eV up to several hundreds of eV in ~10 min was observed in the plasma sheet around 01 hr magnetic local time by two spacecraft at $r \sim 7$ and 9 R_E, respectively, with the spacecraft at larger r observing the dispersion ~20 min earlier than the other. This event occurred during the growth phase of a small non-storm time substorm. Observations in the ionosphere and ground in the vicinity of the spacecraft's footprint indicate that the magnetospheric convection and field-aligned currents (FACs) were enhanced and there was an indication of upward field-aligned potential associated with FACs. We propose that enhanced Poynting flux associated with enhanced convection first drove ~20 eV outflow ions to the plasma sheet to cause the initial enhancement, then the increasing intensities of FACs and the associated upward field-aligned potential gradually increased the energy of the outflow ions to above 100 eV, thus resulting in the observed energy-dispersive enhancement with increasing energy. In addition, the earthward penetration of FACs may explain why the enhancements were observed at larger r earlier.

1. Introduction

The solar wind and the ionosphere are the two particle sources for the Earth's magnetosphere. In the near-Earth magnetosphere, observations have shown that ions upflowing from the ionosphere, mainly H^+, He^+, and O^+ ions, can form cold (<~10 eV) ions inside the plasmapause and warm (~10–1,000 eV) field-aligned ions outside the plasmapause (e.g., Chappell et al., 2008). These two ion populations of the ionospheric source are distinguished from the hot (from ~1 keV to 10's keV) isotropic plasma sheet ions and energetic (>~20 keV) ring current ions that are a mixture of the solar wind and ionosphere sources. Their differences in the energy ranges and pitch-angle distribution types are a result of different transport, energization, and pitch-angle scattering processes.

The warm field-aligned ions are either unidirectional or bidirectional (e.g., Borovsky et al., 2013; Chappell et al., 2008; Giles et al., 1994; Horwitz & Chappell, 1979; Hull et al., 2021; Nagai et al., 1983). Statistically, the unidirectional field-aligned warm ions are more frequently observed on the nightside plasma sheet and at relatively larger radial distances, while the bidirectional field-aligned warm ions appeared more often in the region from the nightside to the dayside and at relatively smaller distances. The bidirectional field-aligned warm ions are termed "warm plasma cloak" because of the cloak shape of their spatial distributions draping around the plasmasphere. The unidirectional field-aligned warm ions are more transient and are observed more often during higher Kp levels, while warm plasma cloak ions are more persistent and appear more frequently with decreasing Kp (Nagai et al., 1983). The warm field-aligned ions come from the ionosphere within the auroral zone, are transported sunward along open trajectories in the plasma sheet by electric and magnetic drift, and are adiabatically energized to the warm ion energies. These transport and energization processes have been investigated with test-particle tracing simulations and can account for the main features of the statistical occurrence probabilities of the warm field-aligned ions (Chappel et al., 2008). In addition, non-adiabatic processes along the field lines connecting the auroral zone and plasma sheet, such as interaction with dispersive Alfvén waves (e.g., Chaston et al., 2015) and acceleration by field-aligned potential (e.g., Maggiolo, 2015), can also contribute to the energization in the field-aligned direction.

Recently, event observations at $L < \sim 6$ (Chaston et al., 2015; Gkioulidou et al., 2019, Hull et al., 2019, Kistler et al., 2016; Nosé et al., 2016, 2021) have shown that transient enhancements of warm field-aligned ions are on a time scale from a few minutes to tens of minutes and can exhibit an energy-dispersion signature. For example, Gkioulidou et al. (2019) reported an event of field-aligned warm O^+ ion enhancements during a geomagnetic storm and the expansion phase of a substorm that had an energy-dispersive signature with decreasing energy from ~1,000 eV down to 10 eV in about 30 min. They compared the observations with a test-particle tracing simulation and concluded that the particular energy-dispersive signature is due to the higher energy ions coming out of the ionosphere, and reaching the spacecraft at the equator earlier than the lower energy ions.

In this paper, we present an event of energy-dispersive field-aligned warm ion enhancements with increasing energy that is opposite from that reported by previous studies, such as Gkioulidou et al. (2019) and Nosé et al. (2016, 2021), and thus cannot be explained by the same process for the outflow ions proposed previously. Investigating this event is thus important to advance our understanding of the different processes contributing to the dynamics of outflow ions and the resulting warm ions. We propose that the increasing energy signature in this event is due to that intensifying upward field-aligned potential gradually increased the energy of outflow ions, based on our analysis of the observed plasma sheet and ionospheric conditions presented below. The observational data are described in Section 2. We present the details of the enhancements and our analysis in Section 3 and discuss the likely underlying processes in Section 4. We summarize our findings in Section 5.

2. Data

For this event, the plasma sheet data are from Time History of Events and Macroscale Interactions during Substorms (THEMIS, Angelopoulos, 2008), the ionosphere data are from Super Dual Auroral Radar Network (SuperDARN) and Defense Meterological Satellite Program (DMSP), the ground data are from magnetometer stations, and the solar wind data are from OMNI and Geotail (Nishida, 1994). In addition, the *AE* index (Davis & Sugiura, 1966) is used for indicating substorm activity.

For the THEMIS data, we use the observations from two THEMIS probes, TH-D and TH-E. The THEMIS orbits are near the equatorial plane with an apogee of $r \sim 14$ R_E and an orbital period of ~23 hr. Ions and electrons measured by ElectroStatic Analyzer (ESA, 0.006–20 keV/q for ions and 0.007–26 keV for electrons) (McFadden et al., 2008) data in "reduced mode" with 3–4 s resolutions are used. Note that ESA cannot distinguish ion species. For particle fluxes, a minimum of one count threshold is applied. For the flux pitch-angle distributions, we define pitch angle (α) to be 0° to 90° for $v_{\parallel} > 0$ and $v_{\perp} > 0$, 90° to 180° for $v_{\parallel} < 0$ and $v_{\perp} > 0$, 0° to −90° for $v_{\parallel} > 0$ and $v_{\perp} < 0$, and −90° to −180° for $v_{\parallel} < 0$ and $v_{\perp} < 0$, where $v_{\parallel}$ ($v_{\perp}$) is particle's parallel (perpendicular) velocity. The omnidirectional flux is averaged over all pitch angles. The THEMIS magnetic field data at 4s resolutions are measured by the flux gate magnetometer (Auster et al., 2008). For the SuperDARN data, the cross polar-cap potential data and the line-of-sight velocities measured at the SANAE station are used. For the DMSP, the measurements from F16 are used. The DMSP satellites are in polar Sun-synchronous circular orbits with high inclination (98°) at 840 km altitude and an orbital period of ~101 min. Electron and ion precipitation fluxes from 30 eV to 30 keV (sample per 1 s) are measured by Special Sensor J (SSJ; Hardy et al., 1984; Meng & Kroehl, 1977). Other DMSP data used include the ionospheric horizontal drift flow speeds (positive for sunward flows) are measured by Special Sensor for Ions Electrons and Scintillation (SSIES; Rich, 1994) Ion Drift Meter (IDM; Heelis & Hanson, 1998) (sample per 1 s), the magnetic field vectors by Fluxgate magnetometer (Merayo et al., 2008; Rich, 1984), and the auroral images by SSUSI (Spectral Sensor Ultraviolet Spectrographic Imager) (Paxton et al., 2018). The ground magnetic fields measured at the M81-338 and M93-347 stations from British Antarctic Survey (BAS) with 1 min resolutions provided through SuperMAG (Gjerloev, 2012) are used (note that the SuperMAG code name is B14 for M81-338 and B16 for M83-347). For Geotail, the magnetic fields measured by Magnetic Field Experiment (Kokubun et al., 1994) are used. The OMNI solar wind data have been propagated to the Earth's bow shock nose.

3. Event Observation

3.1. Event Overview

We investigate an event on 27 December 2017 when the two THEMIS probes, TH-E and TH-D, in the plasma sheet observed field-aligned warm ion enhancements that were energy-dispersive with increasing energy. TH-D

10.1029/2022JA031252

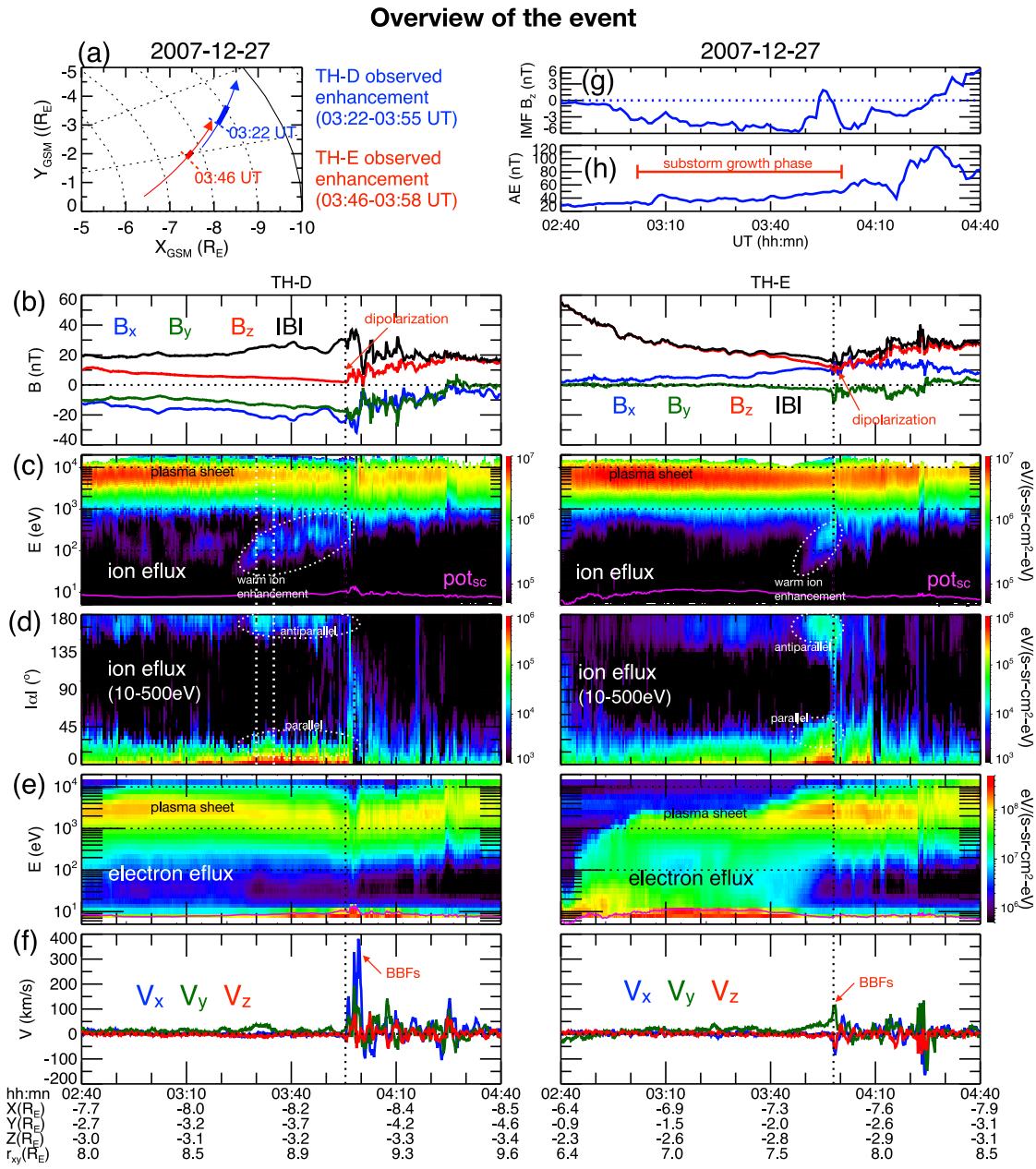

Figure 1. THEMIS observation on 27 December 2007. (a) X-Y projections of the spacecraft trajectories (thin lines) with the intervals of enhancements indicated by thick lines. Temporal profiles of TH-E (left), TH-D (right) for (b) magnetic field components, (c) ion omnidirectional energy fluxes, (d) average energy fluxes of 10–500 eV ions as a function of the absolute value of pitch angle, (e) electron omnidirectional energy flux (the magenta line in (c, e) indicates spacecraft potential, pot_{sc}), (e) ion bulk flow velocities. (g) OMNI IMF Bz. (h) The AE index.

at larger r ($r^2 = X^2 + Y^2$ is the equatorial radial distance) observed the dispersion earlier than did TH-E at smaller r. The enhancements occurred during the growth phase of a substorm when global convection was enhanced. Figure 1 gives an overview of the event. The thin lines in Figure 1a show the X-Y projection of the trajectories of TH-E and TH-D from 02:40 to 04:40 UT with the intervals of enhancements indicated by thick lines. Both probes were in the post-midnight sector around 01 hr MLT moving outward, with TH-D going from r ~8 to 10 R_E and TH-E farther inside going from r ~6 to 8 R_E. From the magnetic fields shown in Figure 1b, TH-D was below the current sheet ($B_x < 0$) while TH-E was above the current sheet ($B_x > 0$). Figures 1c and 1e show the energy spectrum of omnidirectional energy fluxes for ions and electrons, respectively. The spacecraft potential was ~10 V, as indicated by the magenta line and the label (pot_{sc}). Both probes were within the ion plasma sheet

as indicated by the peak of the ion energy fluxes at ~5–10 keV, which is the typical plasma sheet ion thermal energies observed by THEMIS (Wang et al., 2011). TH-D was within the electron plasma sheet as indicated by the peak of the electron energy fluxes at ~2–5 keV, which is the typical plasma sheet electron thermal energy. On the other hand, TH-E entered the electron plasma sheet at ~03:00 UT as indicated by the peak of electron energy flux at < 10 eV. Figure 1c shows that there were short periods of substantial flux enhancements in ions below ~500 eV (i.e., warm ions) observed first by TH-D from ~03:20 to 03:55 UT and then later by TH-E from ~03:46 to 03:59 UT (these warm ion enhancements are indicated by the white dotted elongated circles). Figure 1d shows the averaged ion energy fluxes within the 10–500 eV range as a function of the absolute value of pitch angle (α). The warm ion enhancements were seen mainly in the two field-aligned directions, parallel and antiparallel directions (indicated by the white dotted elongated circles). This field-aligned signature indicated that these warm ion enhancements were likely due to an increase in the numbers of outflow ions flowing to the plasma sheet. In Section 3.2 we will use the ion flux distributions observed by TH-D at 03:30 and 03:35 UT (indicated by the two vertical dotted lines in Figures 1c and 1d) as examples to define field-aligned fluxes and field-aligned types. The warm ion enhancements show an energy-dispersion signature with increasing energy for ~10 min. We will analyze the dispersion in Section 3.3 and show that the dispersions observed by TH-D and TH-E at different times were qualitatively similar. The warm ion enhancements ended abruptly at around 03:55–03:57 UT (indicated by the vertical dotted line) when both probes observed magnetic field dipolarization (indicated by the B_z sharp increase in Figure 1b) and bursty bulk flows (BBFs) (indicated by the sharp increase in bulk flow speeds to above 100 km/s in Figure 1f), which are two main substorm onset signatures. As shown in Figure 1h, the peak AE after the substorm onset only reached ~120 nT, indicating that it was a small substorm. Thus, the enhancements occurred during the substorm growth phase (indicated by the red horizontal line in Figure 1h). The Dst in the past 24 hr varied within −10 and +10 nT (not shown), indicating that it was a non-storm time. As indicated by the OMNI IMF B_z shown in Figure 1g (OMNI data has been propagated to the bow shock nose), the enhancements occurred during a southward IMF condition, thus the global convection was enhanced. We investigate the convection, field-aligned currents (FACs), and field-aligned potential in Section 3.4 using observations in the ionosphere and the ground. With these corresponding observations, we propose in Section 4 that the warm ion enhancements in the plasma sheet were a result of an increase of outflow ion fluxes driven by enhanced convection, and that the energy-dispersion signature with increasing energy was a result of a gradual increase of outflow ion energy due to the acceleration by upward field-aligned potential.

3.2. 2D Pitch Angle Distribution and Field-Aligned Types

In this section, we show that the warm ion fluxes during this event were highly field-aligned, and we define fluxes along different directions (parallel, antiparallel, and perpendicular) and field-aligned types as a function of energy to quantify the flux enhancements. To demonstrate our procedures and definitions, we show in Figure 2 two examples of 2D particle distributions observed by TH-D during the enhancement arbitrarily chosen at 03:30 and 03:35 UT (indicated by the two vertical dotted lines in Figures 1c and 1d). Figure 2a shows the 2D particle distributions of the ion energy fluxes (j) as a function of $E_{\parallel}$ (the x-axis, $E_{\parallel} = (1/2)mv_{\parallel}^2$, where m is the proton mass) and $E_{\perp}$ (the y-axis, $E_{\perp} = (1/2)mv_{\perp}^2$). The positive (negative) $E_{\parallel}$ corresponds to positive (negative) $v_{\parallel}$, and positive (negative) $E_{\perp}$ corresponds to positive (negative) $v_{\perp}$. The particle's energy is $E = (E_{\parallel}^2 + E_{\perp}^2)^{1/2}$.

Our procedures and definitions (see Table 1) are the following,

(I) From the 2D particle distribution, we compute four energy flux values as a function of E within four different pitch-angle ranges: (a) Parallel energy fluxes, $j_{\parallel(+)}$, is the maximum j value within $|\alpha| \le 15°$. (b) Antiparallel energy fluxes, $j_{\parallel(-)}$, is the maximum j value within $165° \le |\alpha| \le 180°$. (c) Perpendicular energy fluxes, $j_{\perp}$, is the maximum j value within $75° \le |\alpha| \le 105°$. (d) Omnidirectional energy flux, $j_{\rm omni}$, is the averaged j value over all α. Note that the absence of perpendicular fluxes at <~500 eV is that their fluxes were below the minimum of one count threshold we applied. The left panel of Figure 2b compares $j_{\parallel(+)}$ (red line), $j_{\parallel(-)}$ (blue line), and $j_{\rm omni}$ (black line) as a function of E at 03:30 UT.

(II) We define three field-aligned types: (a) Bi-directional ($\rm Type_{Bi}$) is $j_{\parallel(+)} \ge 2{\cdot}j_{\rm omni}$ and $j_{\parallel(-)} \ge 2{\cdot}j_{\rm omni}$; (b) one-directional in the parallel direction ($\rm Type_{Para}$) is $j_{\parallel(+)} \ge 2{\cdot}j_{\rm omni}$ and $j_{\parallel(-)} < 2{\cdot}j_{\rm omni}$; (c) one-directional in the antiparallel direction ($\rm Type_{Anti}$) is $j_{\parallel(+)} < 2{\cdot}j_{\rm omni}$ and $j_{\parallel(-)} \ge 2{\cdot}j_{\rm omni}$. Note that the use of the factor of 2 is loosely based on Chappell et al. (2008) and they regarded the bi-directional warm ions as "warm plasma cloak." Also note that in our definition for $\rm Type_{Bi}$, $j_{\parallel(+)}$ and $j_{\parallel(-)}$ do not need to be the same. For example, in the left panel of Figure 2b, the values of $j_{\parallel(+)}$ and $j_{\parallel(-)}$ between ~30 and 400 eV were at least a factor of

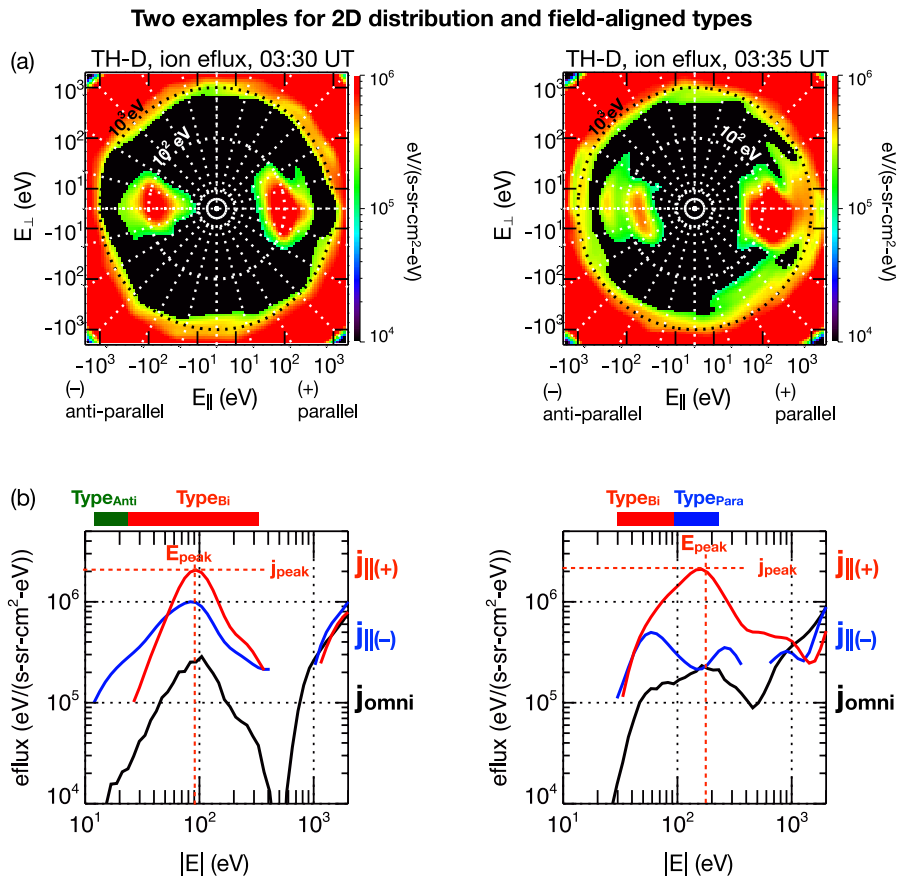

Figure 2. (a) 2-D distributions of ion energy fluxes as a function of ion energy (for $\pm v_{\parallel}$ in the x-axis and $\pm v_{\perp}$ in the y-axis) and (b) comparisons of $j_{\parallel(-)}$, $j_{\parallel(+)}$, and j_{omni} as a function ion energy observed by TH-D at 03:30 UT (left panels) and 03:35 UT (right panels). The field-aligned type of warm ions is indicated by the bars on the top (b) (red bars for Type_{Bi}, blue for $\text{Type}_{\text{Para}}$, and green for $\text{Type}_{\text{Anti}}$).

Table 1
Definition of Symbols

Symbol	Definition
α	Pitch angle
j	Energy flux
$j_{\parallel(+)}$	Parallel energy flux: the maximum j value within $\lvert\alpha\rvert \le 15°$
$j_{\parallel(-)}$	Anti-parallel energy fluxes: the maximum j value within $165° \le \lvert\alpha\rvert \le 180°$
$j_{\perp}$	Perpendicular energy fluxes: the maximum j value within $75° \le \lvert\alpha\rvert \le 105°$
j_{omni}	Omnidirectional energy flux: the averaged j value over all α
j_{peak}	The peak energy fluxes for ions between 10 and 1,000 eV
E_{peak}	The energy corresponding to the j_{peak}
Type_{Bi}	Bi-directional type: $j_{\parallel(+)} \ge 2{\cdot}j_{\text{omni}}$ and $j_{\parallel(-)} \ge 2{\cdot}j_{\text{omni}}$
$\text{Type}_{\text{Para}}$	One-directional in parallel direction type: $j_{\parallel(+)} \ge 2{\cdot}j_{\text{omni}}$ and $j_{\parallel(-)} < 2{\cdot}j_{\text{omni}}$
$\text{Type}_{\text{Anti}}$	One-directional in antiparallel direction type: $j_{\parallel(+)} < 2{\cdot}j_{\text{omni}}$ and $j_{\parallel(-)} \ge 2{\cdot}j_{\text{omni}}$
λ_{B}	Magnetic field elevation angle: $\lambda_{\text{B}} = \text{asin}(\lvert B_z\rvert/\lvert B\rvert)$
$\Phi_{\parallel}$	Field-aligned potential
pot_{sc}	Spacecraft potential

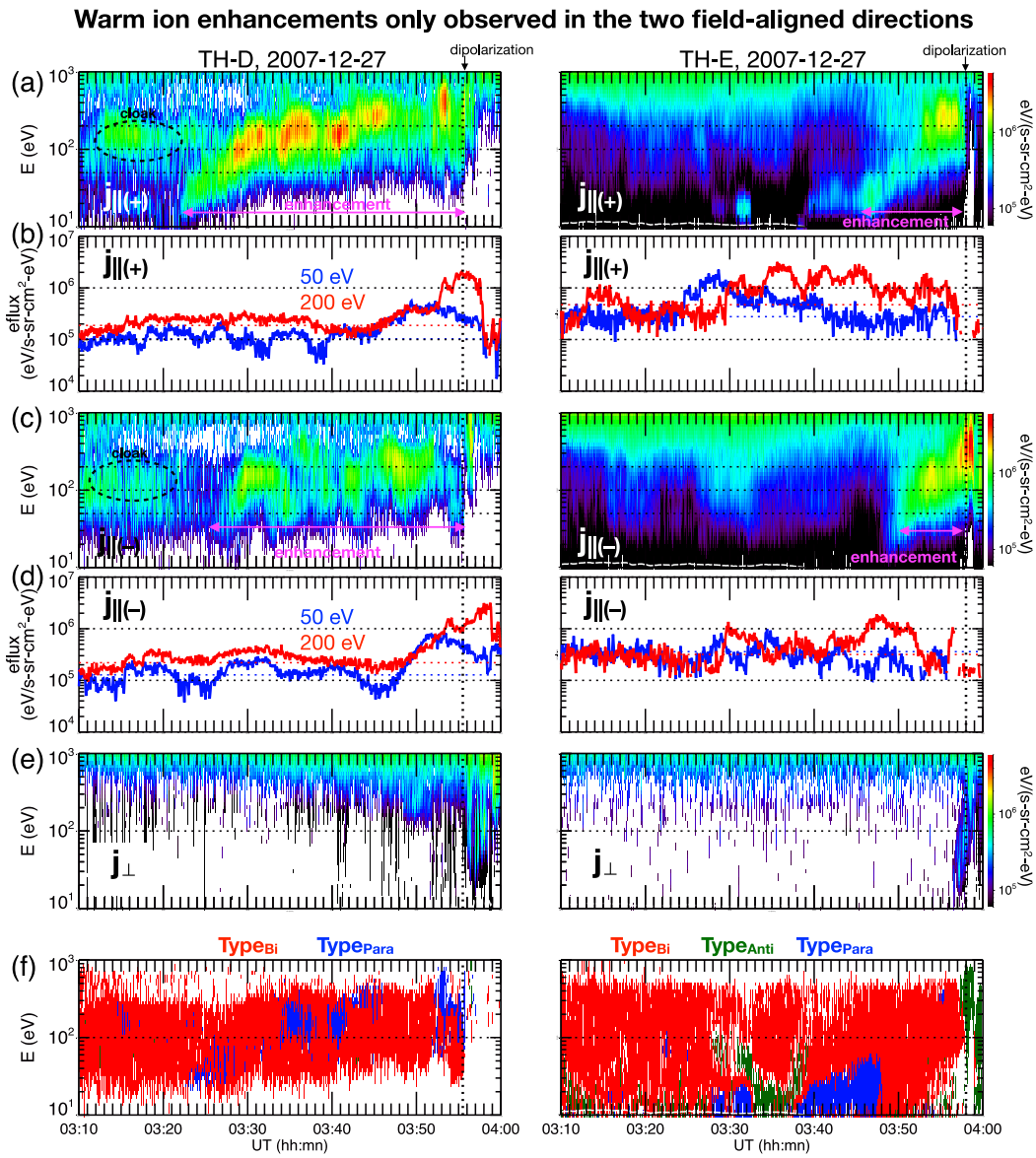

Figure 3. Ion fluxes observed by TH-D (left panels) and TH-E (right panels) on 27 December 2007. (a) Energy spectrum of ion energy flux in the parallel direction ($j_{\|(+)}$). (b) $j_{\|(+)}$ profiles for 50 and 200 eV. (c) Energy spectrum of ion energy flux in the antiparallel direction ($j_{\|(-)}$). (d) $j_{\|(-)}$ profiles for 50 and 200 eV. (e) Energy spectrum of ion energy flux in the perpendicular direction ($j_{\perp}$). (f) Energy spectrum of the field-aligned types.

2 higher than j_{omni}, indicating that the warm ion enhancements at these energies were $Type_{Bi}$ (indicated by the red bar on the top). In comparison, below 20 eV only $j_{\|(-)}$ was higher than j_{omni}, indicating that at these energies the enhancements were $Type_{Anti}$ (indicated by the green bar). Note that the same color coding used for the bars on the top of Figure 2b to indicate different field-aligned types will be used again in Figure 3f.

(III) In addition, from the *j*-*E* distribution shown in Figure 2b, for both $j_{\|(+)}$ and $j_{\|(-)}$, we define j_{peak} as the peak energy fluxes for ions between 10 and 1,000 eV (indicated by the red horizontal dotted line for $j_{\|(+)}$) and E_{peak} (indicated by the red vertical dotted line for $j_{\|(+)}$) as the energy corresponding to the j_{peak}.

Another example is shown in the right panels of Figures 2a and 2b for the TH-D observation 5 minutes later at 03:35 UT. $Type_{Bi}$ flux enhancement was mainly seen below ~100 eV, while $Type_{Para}$ flux enhancement was mainly seen in ~100–200 eV (indicated by the blue bar on the top). Note that at ~100 eV, $j_{\|(+)}$ was substantially larger than $j_{\|(-)}$, but their values were all larger than $2 \cdot j_{omni}$ so the corresponding type was $Type_{Bi}$.

3.3. Field-Aligned Enhancements and Energy-Dispersive Signature

In this section, we show in Figures 3–5 that the energy-dispersive flux enhancements observed first by TH-D and later by TH-E were quantitatively similar in that their energy increased from ~20 to ~200 eV in ~10 min. We first show that the flux enhancements were only field-aligned, indicating that these warm ions were outflow ions transported to the plasma sheet. Figures 3a, 3c, and 3e show the energy spectrum of $j_{\parallel(+)}$, $j_{\parallel(-)}$, and $j_{\perp}$, respectively, observed by TH-D (left panels) and TH-E (right panels). Figures 3b and 3d show the temporal profiles of $j_{\parallel(+)}$ and $j_{\parallel(-)}$, respectively, at 50 eV (blue curve) and 200 eV (red curve). The energy spectrum of the field-aligned types is shown in Figure 3f. Despite that TH-D and TH-E were less than 2 R_E apart, they did not observe warm ion enhancements simultaneously. TH-D first observed pre-existing warm plasma cloak at ~50–300 eV that was well separated from the plasma sheet ions before ~03:20 UT. It then observed several enhancements in warm ions from ~20 eV to several hundreds of eV in both $j_{\parallel(+)}$ and $j_{\parallel(-)}$ but not in $j_{\perp}$ from ~03:22 to ~03:55 UT (indicated by the horizontal magenta line). The enhancements stopped around the time when dipolarization started. Details of these enhancements are shown in Figure 4. About 20 min later, TH-E also observed the field-aligned enhancements in warm ions from ~03:46 to 03:58 UT (details shown in Figure 5). These warm ion enhancements were observed in both $j_{\parallel(+)}$ and $j_{\parallel(-)}$, thus they were mainly Type_{Bi} as shown in Figure 3f. Since the energy range of ~20–500 eV for these enhancements was close to the typical characteristic energy of 30–1,200 eV for outflow H^+ ions observed near 6,000 km altitude in the midnight auroral zone during quiet time (Peterson et al., 2008), we argue that these field-aligned warm ion enhancements observed by TH-D and TH-E were a result of an increase in the numbers of outflow H^+ ions flowing to the equatorial plasma sheet along the magnetic field lines.

Here we show that energy-dispersive enhancements observed by TH-D and TH-E at different times were quantitatively similar. We first show in Figures 4 and 5 the variations of E_{peak} and j_{peak} (defined in Section 3.2 and Figure 2b) for TH-D and TH-E, respectively. In Figures 4 and 5 we only plot $j_{\parallel(+)}$ and $j_{\parallel(-)}$ for the times and energies where the energy fluxes were enhanced so that the features associated with the flux enhancements can be more clearly shown. Here we define that the energy flux at a given time and energy was enhanced if the flux value was a factor of 2 higher than the pre-enhancement flux value. The pre-enhancement flux value at a given energy is defined as the averaged energy fluxes over the pre-enhancement interval, 03:10 to 03:20 UT, at that energy (e.g., see the energy fluxes for 50 and 200 eV shown in Figures 3b and 3d). The E_{peak} values for $j_{\parallel(+)}$ in Figures 4a and 5a and $j_{\parallel(-)}$ in Figures 4b and 5b are indicated by black lines. The differences in the features between the two field-aligned directions are shown by comparing $j_{\parallel}$ in Figures 4c and 5c and by comparing j_{peak} in Figures 4d and 5d. Figures 4a and 4b show that the enhancements observed by TH-D from ~03:20 to 03:55 UT consisted of five pairs of short enhancements in $j_{\parallel(+)}$ (indicated by p1-p5 in Figure 4a with "p" standing for parallel fluxes) and $j_{\parallel(-)}$ (indicated by a1–a5 with "a" standing for antiparallel fluxes). For the first enhancement of our interest (p1-a1), the dispersion has the signature with increasing energy (E_{peak} increasing in time, as indicated by magenta tilted upward-pointing arrows in Figures 4a and 4b), the enhancement in $j_{\parallel(+)}$ appeared earlier than in $j_{\parallel(-)}$, the two highest E_{peak} values were similar (Figure 4c), and the j_{peak} values were similar (Figure 4d). In comparison, as shown in Figure 5, TH-E also observed dispersive enhancements from ~03:46 UT with the signature of increasing energy observed in both $j_{\parallel(+)}$ and $j_{\parallel(-)}$ (indicated by magenta tilted upward-pointing arrows in Figures 5a and 5b) with similar E_{peak} (Figure 5c) and j_{peak} values (Figure 5d). Comparing Figures 4 and 5 shows that this enhancement observed by TH-E at ~03:46 UT was quantitatively similar to the first enhancement observed by TH-D at ~03:22 UT (the p1 enhancement) in the duration (~10 min), the dispersion signature (increasing energy), the E_{peak} range (from ~20 eV to ~150–200 eV), and the j_{peak} range (~$5{\cdot}10^1$ to ~$3{\cdot}10^2$ eV/(s-sr-cm^2-eV). In Section 4, we propose this time delay between TH-D and TH-E in observing the very similar dispersive enhancement was due to that the driver for the enhancement, that is, enhanced convection, penetrated earthward and reached the TH-D location earlier.

3.4. Corresponding Observations in Solar Wind, Ionosphere, Ground, and Plasma Sheet

In this section, we show that, when field-aligned warm ion enhancements were observed in the plasma sheet, the observations in the ionosphere and the ground conjugated with TH-D and TH-E indicated that the ionospheric convection was enhanced and extended equatorward, region-2 FACs were enhanced, and the existence of upward field-aligned potential. Figure 6 shows the ionospheric convection flows observed by SuperDARN radar and FACs observed by ground magnetometers. Figure 6a shows the IMF B_y (blue) and IMF B_z observed by Geotail in front of the bow shock at $X \sim 28$ R_E. The Geotail observations confirmed that the OMNI IMF B_z shown in

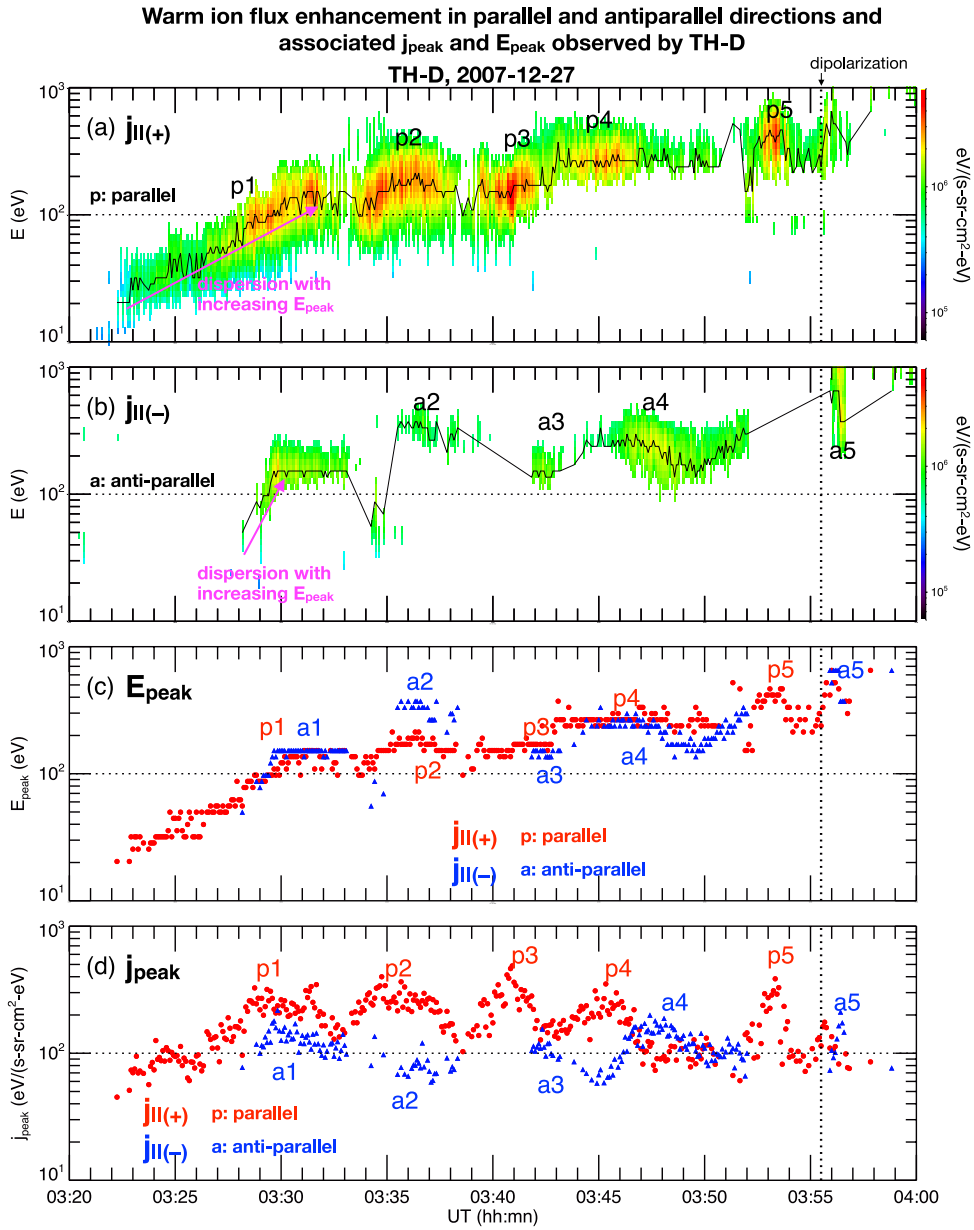

Figure 4. Ion fluxes observed by TH-D on 27 December 2007. (a) Energy spectrum of ion energy flux in (a) the parallel direction ($j_{\parallel(+)}$) and (b) antiparallel direction ($j_{\parallel(-)}$) (only the data satisfying the enhancement criteria are plotted). (c) E_{peak} and (d) j_{peak} of $j_{\parallel(+)}$ and $j_{\parallel(-)}$.

Figure 1g indeed propagated to the Earth. The southward IMF likely impacted the Earth shortly after ~02:50 UT. Figure 6b shows the cross-polar cap potential (Φ_{PC}) (estimated from SuperDARN radar measurements) started to increase quickly from ~30 to 50 kV after ~02:55 UT and the potential remained elevated throughout this event, indicating enhanced global convection (indicated by the magenta arrow) that is typical for the substorm growth phase. Figure 6c shows the line-of-sight (l-o-s) flow speeds measured at a SuperDARN station, SANAE (indicated by the black triangle), on the nightside southern hemisphere in the region around 01 hr MLT and −62 to −70 MLat at three different times. The positive (negative) l-o-s speeds are ionospheric flows toward (away) the station, thus were equatorward (poleward) at these UT times. The radar coverage at the time was close to the ionospheric footprints of TH-E (red unfilled square) and TH-D (blue unfilled square) estimated using the Tsyganenko 96 (T96) magnetic field model (Tsyganenko, 1995, 1996). It can be seen that the region of enhanced equatorward flow (reddish colors) penetrated equatorward with time. This equatorward penetration of

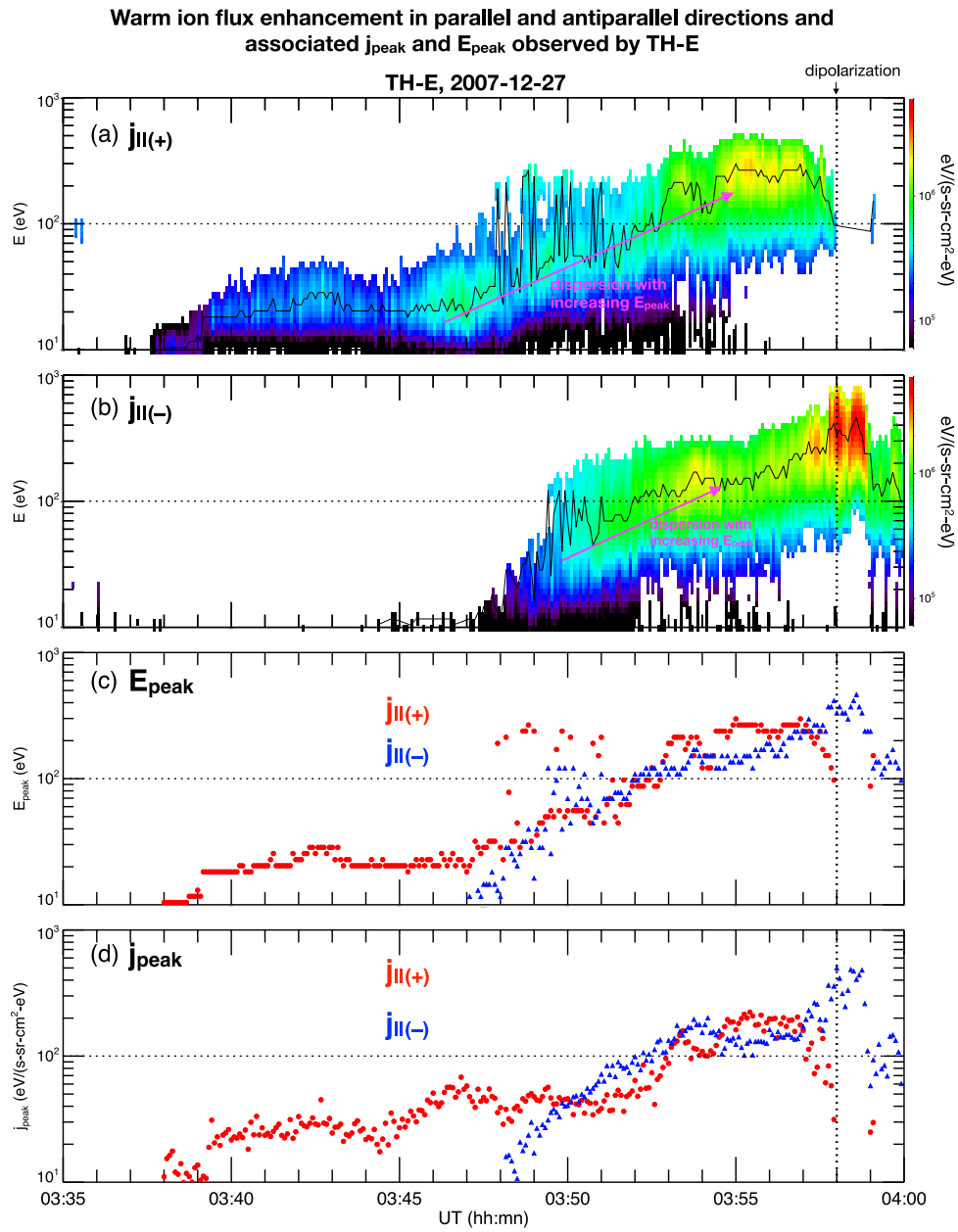

Figure 5. Ion fluxes observed by TH-E on 27 December 2007. (a) Energy spectrum of ion energy flux in (a) the parallel direction ($j_{\parallel(+)}$) and (b) antiparallel direction ($j_{\parallel(-)}$) (only the data satisfying the enhancement criteria are plotted). (c) E_{peak} and (d) j_{peak} of $j_{\parallel(+)}$ and $j_{\parallel(-)}$.

enhanced ionospheric convection can be more clearly seen in Figure 6d showing the l-o-s speeds from one of the 15 scanning beams of the SANAE radar (the beam 7, as indicated by the magenta line in Figure 6c) as a function of time and MLat. The region of enhanced convection was poleward of −70° before ~03:15 UT, then it started to move equatorward at ~03:35 UT to ~−67°. The timing of enhanced convection penetrating to equatorward of ~−70° around midnight is also supported by ground magnetic field perturbations. Figures 6f and 6g show the perturbations observed at the magnetometer station B14 (indicated by the red circle in Figure 6d) and B16 (indicated by the blue triangle in Figure 6d), respectively. The perturbations are in the *N*-*E*-*Z* coordinates (*N* is local magnetic north, *E* is local magnetic east, and *Z* is vertically down). The ground perturbations at the two stations started to enhance at ~03:15 UT. The perturbations were southward and eastward at both stations but vertically downward (upward) at lower (higher) latitudes (indicated by magenta arrows), indicating an enhancement of the

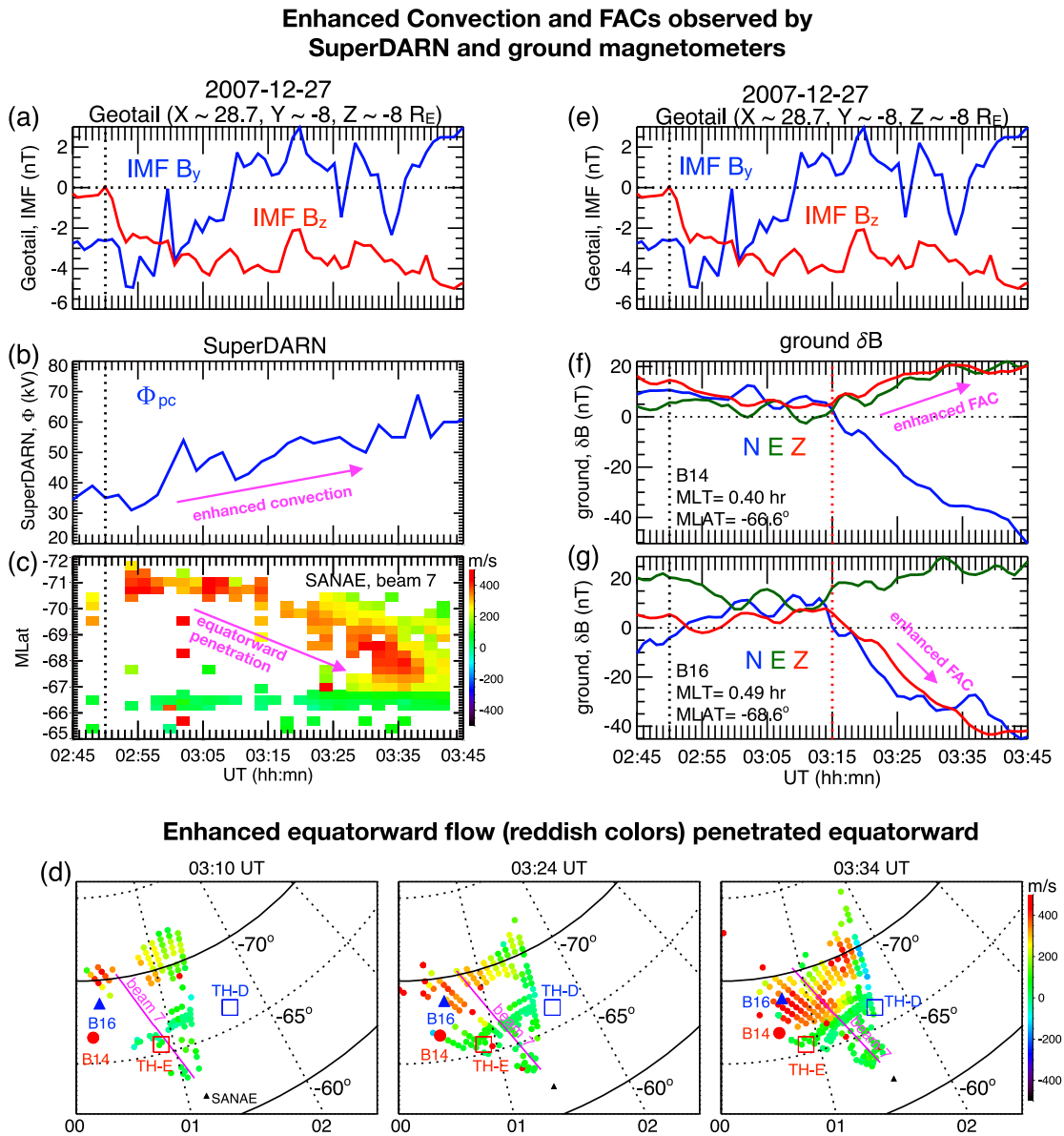

Figure 6. (a, e) IMF observed by Geotail. (b) Cross polar-cap potential from SuperDARN. (c) Line-of-sight speed measured by the beam 7 of SANAE SuperDARN radar. (d) Line-of-sight speed measured by SANAE radar at three different times. The magenta line indicates the beam 7 of SANAE radar. The locations of B14 and B16 stations and footprints of TH-D and TH-E are indicated. The ground magnetic field perturbations measured at (f) B14 and (g) B16 stations.

westward equivalent current. Such a current enhancement can be associated with enhanced region-2 FACs under enhanced global convection (Lyatskaya et al., 2016). The above observations suggested that the equatorward penetration of the enhanced convection was likely to reach the TH-D location first after around 03:15 UT and then the TH-E location sometime later.

We show in Figure 7 the existence of upward field-aligned potential associated with upward FACs observed by DMSP during the warm ion enhancements observed in the plasma sheet. Figure 7 shows the aurora in the southern hemisphere observed by DMSP F16 SSUSI UVI imager around 03:22 UT. The equatorward edge of the aurora was at ~−66° at 00 MLT and ~−67° at 02 MLT. From the estimated ionospheric footprints, at the time TH-E was likely equatorward of the aurora while TH-D was within the aurora. Figures 7b–7e show the F16 measurements from 03:23 to 03:24 UT (the F16 trajectory during this one-minute interval is indicated by the two magenta dots connected with a magenta line in Figure 7a). The negative horizontal flow (Figure 7b) indicates equatorward flow, consistent with the SuperDARN flows shown in Figure 6c. Figure 7c shows the magnetic field

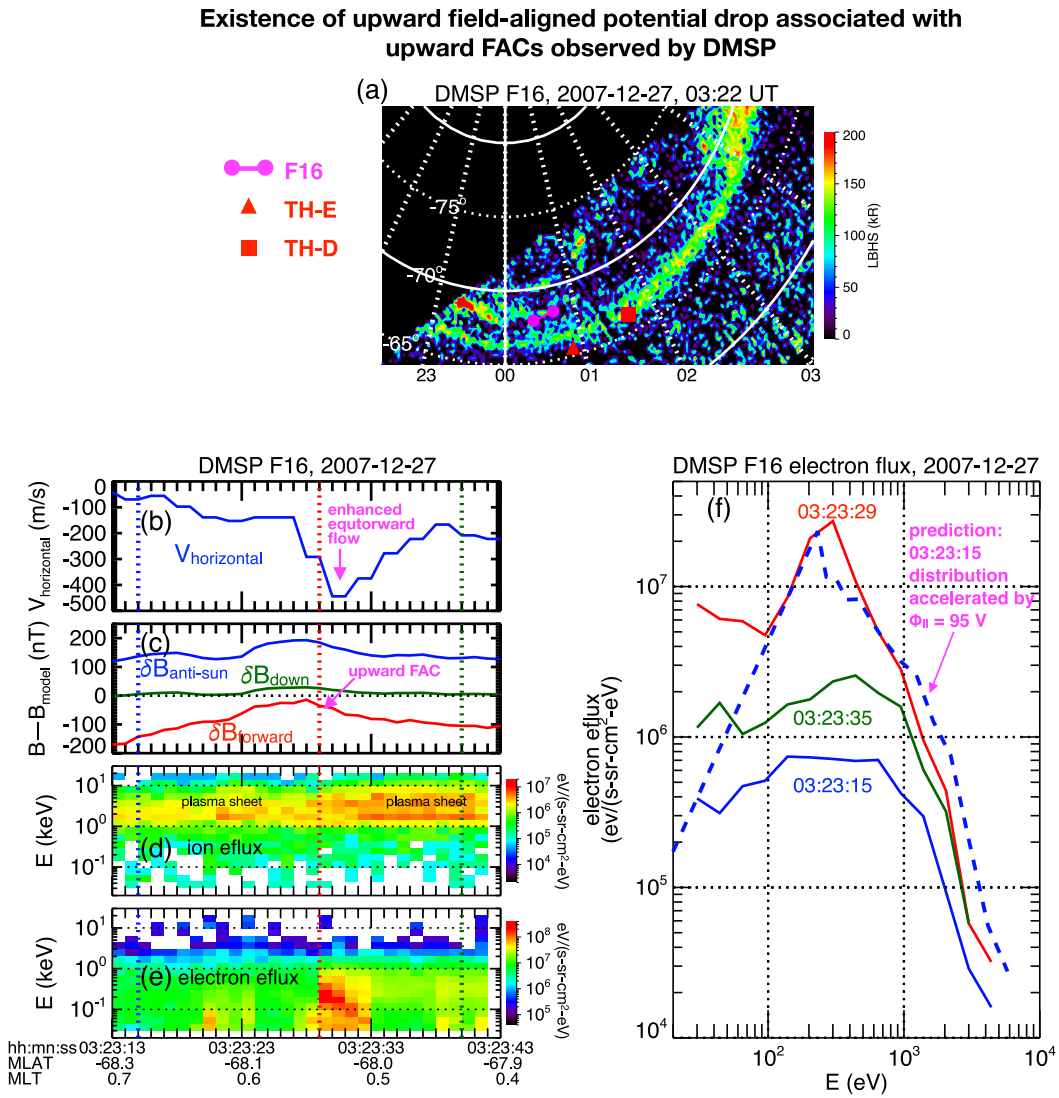

Figure 7. Defense Meterological Satellite Program F16 measurements on 27 December 2007. (a) SSUSI aurora image. The footprints of F16, TH-E, and TH-D are indicated. (b) Ion horizontal flow (negative is anti-sunward). (c) The magnetic field difference from the IGRF fields in the downward direction (green), spacecraft forward direction (red), and anti-sunward direction (blue). Energy spectrum of (d) ion and (e) electron energy fluxes. (f) Electron fluxes at three different times. The blue dashed curve is the prediction for the flux at 03:23:15 UT (blue curve) to be accelerated by $\Phi_{||} = 95$ V.

perturbations from the IGRF magnetic field model. The changes in the directions of the slopes in the magnetic field perturbations in the two horizontal components (the anti-sunward component in blue and the forward component along the spacecraft trajectory in red) from increasing to decreasing around 03:23:29 UT (indicated by the vertical red dotted line) indicate the presence of upward FACs. Figures 7d and 7e show the energy spectrum of energy fluxes for ions and electrons, respectively. The ion energy spectrum had the peak energy of a few keV, which is typical for geomagnetic active plasma sheet observed by DMSP SSJ (Wing & Newell, 1998). Figure 7f shows the electron energy fluxes versus energy at three different times indicated by vertical dotted lines in Figures 7b–7e with different colors (03:23:15 UT in blue, 03:23:29 UT in red, and 03:23:35 UT in black). Figure 7f shows that the spectrum shape at 03:23:29 UT was significantly different from those of the other two spectra before and after, suggesting that the electrons at 03:23:29 UT were accelerated by a quasi-static upward field-aligned potential. We predicted spectrum for the spectrum of 03:23:15 UT (blue curve) under an upward field-aligned potential ($\Phi_{||}$) of 95 V (blue dashed curve) in Figure 7f, the consistency between the predicted distribution (blue dashed curve) with the 03:23:29 UT (red) confirms the existence of the upward $\Phi_{||}$. Note that the

low energy electrons (<∼100 eV) do not match the prediction as well because these electrons can be associated with the secondary electrons generated by the initial electron precipitation (Wing et al., 2019). These low energy electrons are expected to have variabilities. As discussed in Section 4, such upward field-aligned potential, which was associated with the upward FACs seen in the magnetic field perturbations shown in Figure 7c, might play a role in accelerating outflow ions to cause the energy-dispersion signature with increasing energy observed by TH-D and TH-E.

Here we show that the magnetic field lines at TH-D and TH-E locations became more stretched during the warm ion enhancements in response to the enhanced convection. Figure 8 shows the plasma sheet magnetic conditions at the two THEMIS locations. Figures 8a and 8b show the E_{peak} and j_{peak} in the parallel direction, respectively (the same as those shown in Figures 4 and 5 for TH-D and TH-E). Figure 8c shows that TH-E and TH-D were moving outward. Figure 8d shows the magnetic field components and Figure 8e shows the magnetic field elevation angle, $\lambda_B = \text{asin}(|B_z|/|B|)$. A smaller λ_B value indicates that the magnetic field lines are more stretched. TH-E observed a clear drop in λ_B at around 03:33 UT. TH-D observed continuous decreases in λ_B, but there was a clear change in the slopes of λ_B and magnetic field strength at ∼03:20 UT with a relatively steeper drop and larger magnetic field strength afterward. These suggest that the magnetic field configuration became more stretched first at the TH-D location ($r \sim 8.5$ R_E) around 03:20 UT and later at smaller radial distances at the TH-E ($r \sim 7.3$ R_E) at 03:33 UT. This sequence is consistent with the enhanced convection moving earthward in the plasma sheet (equatorward in the ionosphere) since enhanced convection causes thinning of the current sheet and magnetic field line stretching. As shown in Figures 8a and 8b, the warm ion enhancements started to appear shortly after the magnetic field configuration became more stretched, suggesting a close connection between the warm ion enhancements and enhanced convection.

Here we show that the strengths of warm ion enhancements were correlated with compressional waves. Figure 8f shows the magnetic field perturbations (obtained by subtracting 10 min running averages) in the parallel direction (red) and the two perpendicular directions (blue and green). Ultralow frequency waves with amplitudes up to ∼2 nT were observed at both THEMIS locations. Interestingly, compressional waves ($\delta B_{\parallel}$) with periods of ∼5 min were observed at TH-D and TH-E from ∼03:25 to 03:50 UT. As indicated by the red vertical dotted lines shown in Figures 8b and 8f for TH-D, there was a good correspondence between $\delta B_{\parallel}$ and the j_{peak} observed by TH-D, suggesting that compressional ULF waves might play a role in modulating the strength of warm ion enhancements.

4. Discussion of Possible Processes for the Enhancement and Energy-Dispersion Signature

Based on our analysis presented above, we propose that the observed field-aligned warm ion enhancements during the growth phase of a substorm were a result of increasing outflow H+ ions driven by enhanced convection and that the dispersion with increasing energy was a result of the outflow ions being gradually accelerated by intensifying upward field-aligned potential. In this section, we discuss possible source and transport (point I), and acceleration (point II) for this event and our proposed processes (point III). We present additional discussion in point IV.

(I) Source and transport: We consider that the warm field-aligned ions observed in the plasma sheet were outflow H^+ ions flowing out of the ionosphere along the magnetic field lines and that the enhancement near the equatorial plane is a sole result of an enhancement in the ionospheric outflow source due to enhanced convection. Increasing Poynting fluxes from the magnetosphere into the ionosphere associated with enhanced ionospheric convection can drive larger number fluxes of outflow ions (e.g., Strangeway et al., 2005). The timing of the start of the enhancements in the field-aligned fluxes at ∼20 eV at the TH-D location near the equator at $r \sim 8$ R_E was about 30 min after the cross polar-cap potential was enhanced (Figure 6b) and ∼10 min after the nightside convection near the TH-D's ionospheric footprint was enhanced (Figures 6c and 6d). For a 20 eV proton at 0° pitch angle ($v_{\parallel} = 62$ km/s), it would take the particle about 15 min to move along the field line at midnight from the top of the ionosphere to the equator (the field line length is ∼9 R_E as estimated by using the T96 magnetic field model). Considering the uncertainty in the exact start time of enhanced convection at the TH-D's exact footprint, such transport time is reasonable to bring the enhanced outflow proton fluxes to the TH-D's location. This transport time also rules out the possibility that the 20 eV ions observed by TH-D were O^+ ions, which would take ∼60 min to arrive. As the

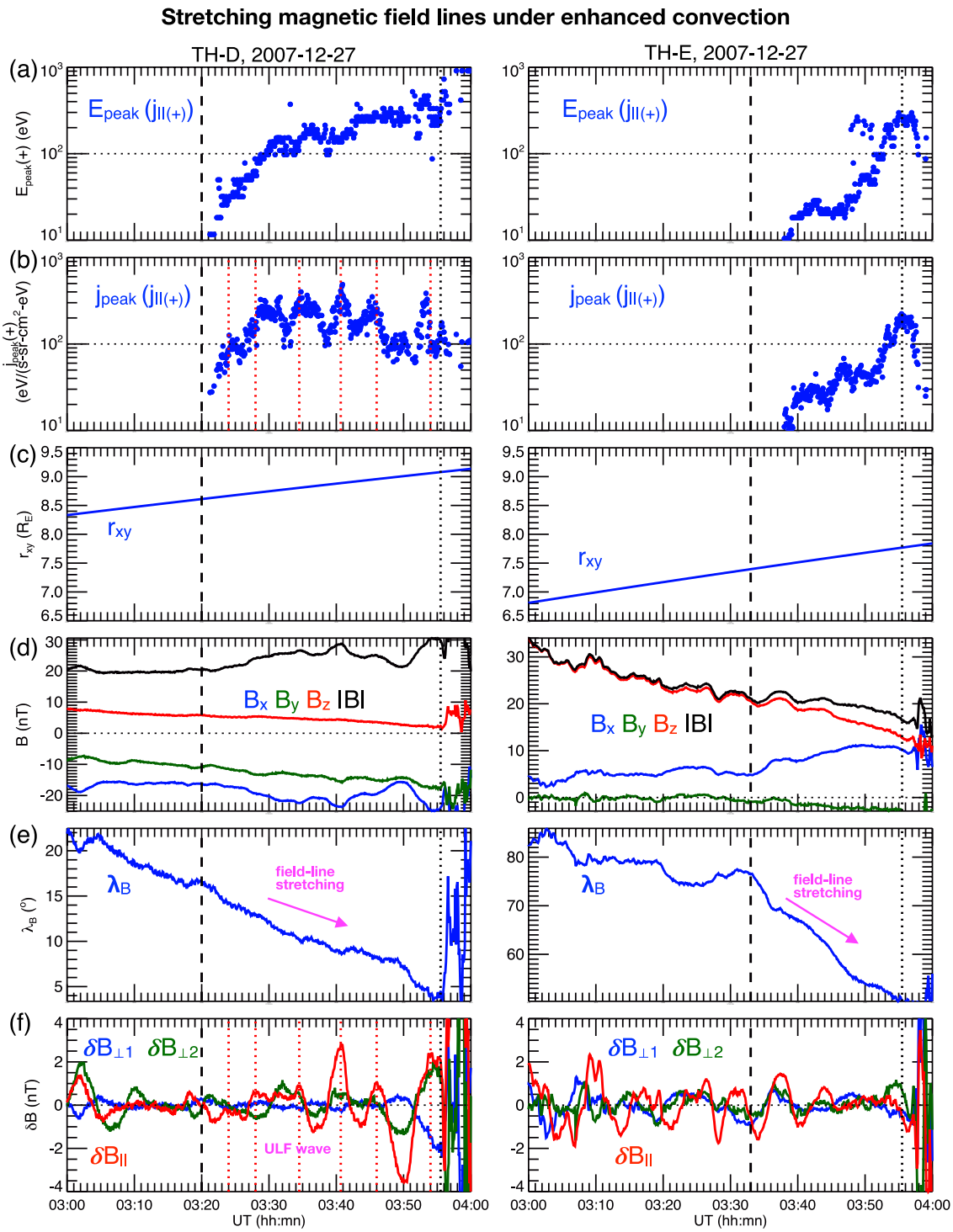

Figure 8. Observations of TH-D (left panels) and TH-E (right panels) on 27 December 2007. (a) E_{peak} and (b) j_{peak} of $j_{\parallel(+)}$, (c) equatorial radial distances, (d) magnetic field components, (e) magnetic field elevation angles, and (f) magnetic field perturbation in the parallel and two perpendicular directions.

equatorward edge of enhanced convection and enhanced Poynting fluxes moved further equatorward in the ionosphere, it increased the outflow fluxes at the latitudes of the TH-E's footprint. This extra equatorward propagation time and the additional particle transport time to the equator can explain why TH-E, ~1 R_E earthward of TH-D, observed the enhancement in the 20 eV ions at a later time than that of TH-D.

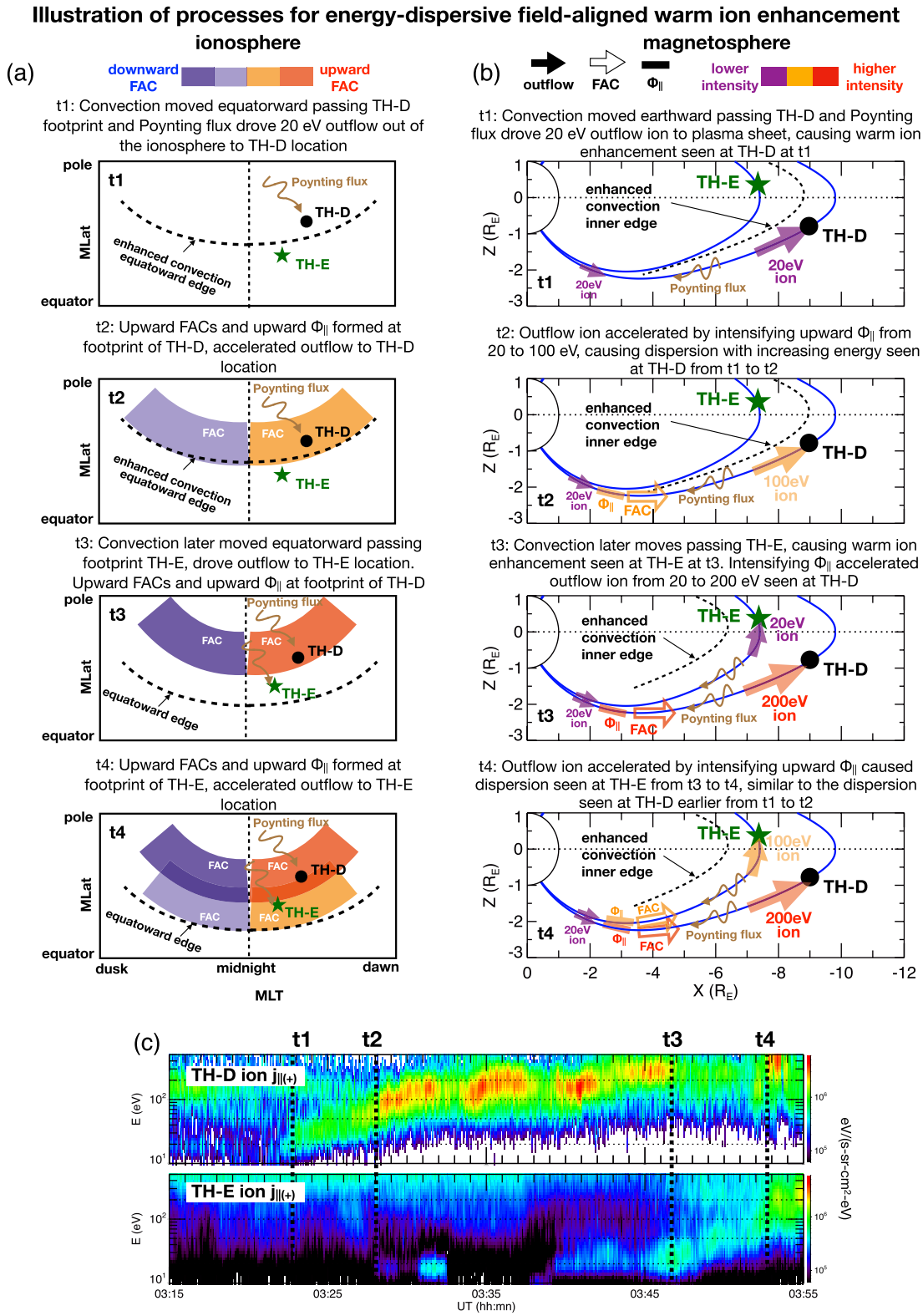

Figure 9.

(II) Acceleration: We consider that the increasing-energy signature of the dispersion was a result of an acceleration of the outflow ions to higher energies by intensifying upward field-aligned potential. Previous studies did not suggest that larger Poynting fluxes into the ionosphere can also result in higher temperatures for the outflow ions. Since the DMSP observation indicates the existence of upward FACs and upward field-aligned potential around the footprints of TH-D and TH-E (Figure 7), here we consider that the upward field-aligned potential associated with upward FACs can increase the temperatures of outflow ions (e.g., Maggiolo, 2015). The field-aligned potential is typically located below 2 R_E. Simulations (e.g., Gkioulidou et al., 2009) and empirical modeling (e.g., Yue et al., 2015) have shown that region-2 FACs are formed in the near-Earth plasma sheet with upward (downward) FACs at the post-midnight (pre-midnight) MLTs. The earthward edge of region-2 FACs moves earthward (equatorward in the ionosphere) under enhanced convection while the strengths of FACs and associated field-aligned potential both increase. This thus suggests that as the intensity of the upward field-aligned potential increases corresponding to intensifying upward FACs, the energy of accelerated outflow ions also increase.

(III) Proposed processes: Based on the above consideration of the possible source, transport, and acceleration, we illustrate in Figure 9 our proposed processes leading to the energy-dispersive field-aligned warm ion enhancements observed by TH-D and TH-E. Figures 9a and 9b show the ionosphere and magnetosphere, respectively, at different times ($t1 < t2 < t3 < t4$). Figure 9a shows the equatorward edge of enhanced convection (black dotted curve) and distributions of R2 FACs (in colors, with the color scale on the top of Figure 9a) in the ionosphere relative to the footprints of TH-D and TH-E. Figure 9b illustrates upward R2 FAC (unfilled arrows), outflow ions (filled arrows), and field-aligned potential (filled blocks) along the magnetic field lines connecting to the TH-D and TH-E locations with their intensities indicated by the color scale on the top of Figure 9b. Note that magnetic field lines should gradually become stretched with time under enhanced convection, but here we plot time-independent magnetic field lines for the simplicity of the illustration. Figure 9c shows the ion energy fluxes along the parallel direction observed by TH-D and TH-E. The proposed processes occurred in the following order:

(1) Before $t1$, the IMF turned southward and global convection was enhanced, the equatorward (earthward) edge of enhanced convection penetrated equatorward (earthward) in the ionosphere (magnetosphere) and upward FACs in the post-midnight sector were enhanced, as supported by the observations shown in Figures 6f and 6g.

(2) At $t1$, the equatorward (earthward) edge passed TH-E but had not reached TH-D. The enhanced Poynting flux drove 20 eV outflow H^+ ions to the equatorial plasma sheet, thus TH-D observed enhancements of 20 eV field-aligned ions at ~03:22 UT (Figure 9c).

(3) From $t1$ to $t2$, upward FACs and upward $\Phi_{\parallel}$ gradually increased and accelerated the outflow ions from 20 to 100 eV, thus causing the dispersion with increasing energy observed by TH-D from ~03:22 to 03:28 UT. Note that the timescale for increasing field-aligned potential is likely slow as compared to the transport time from the ionosphere to the equator for >100 eV protons. If the field-aligned potential increases very quickly and higher energy protons arrive TH-D earlier because of their larger $v_{\parallel}$ speeds as compared to lower energy protons, it would then result in an energy-dispersion signature with decreasing energy like that reported by Gkioulidou et al. (2019).

(4) At $t3$, the equatorward (earthward) edge now passed TH-D and the enhanced Poynting flux drove 20 eV outflow ions out of TH-E footprint, thus TH-E observed enhancements of 20 eV field-aligned ions at ~03:46 UT, ~20 min later than did TH-D.

(5) From $t3$ to $t4$, upward FACs and upward $\Phi_{\parallel}$ at the TH-E footprint gradually increased and accelerated the outflow ions from 20 to 100 eV, which caused TH-E to observe similar energy-dispersion as seen by TH-D 20 min earlier.

(IV) In addition, we discuss possible processes for the end of warm ion enhancements at the start of dipolarization and hemispheric asymmetries. The FACs and associated field-aligned potential within the region of dipolarization and BBFs are expected to be much stronger than the FACs during the growth phase. The field-aligned potential may be above 1 kV and thus is capable of energizing the field-aligned ions to above 1 keV. This may explain why, in this event, the two THEMIS probes no longer observe the enhancements

Figure 9. Illustration of the proposed processes to explain the energy-dispersive field-aligned warm ion enhancements observed by TH-E and TH-D. (a) Region 2 field-aligned currents (FACs) (colors) in the ionosphere from $t1$ to $t4$ ($t1 < t2 < t3 < t4$). The footprint of TH-D (TH-E) is indicated by black dot (green star). The equatorward edge of enhanced convection indicated by black dotted curve). (b) Different quantities in the X-Z plane along the 01 hr MLT from $t1$ to $t4$. The magnetic field lines are indicated by blue curves and the location of TH-D (TH-E) is indicated by black dot (green star). The inner edge of enhanced convection is indicated by black dotted curve, Poynting flux by brown wavy arrow, outflow ions by filled arrow, FACs by unfilled arrow, and field-aligned potential ($\Phi_{\parallel}$) by filled block, The color scale for these symbols indicates their intensity.

in the field-aligned ions below 1 keV when encountering dipolarization and BBFs. For this event, the enhancements were relatively larger in the parallel direction than in the antiparallel direction, indicating a hemispheric asymmetry. The low-latitude observations in the vicinity of the footprints of TH-D and TH-E were mainly available for the southern hemisphere during this event, thus, we do not have sufficient observations in both hemispheres to evaluate plausible explanations for the asymmetry. This event was in December when the ionospheric conductance could have stronger hemispheric asymmetry, which might contribute to asymmetries in the magnetosphere-ionosphere coupling and the resulting convection strength and FAC strength. This speculation needs to be further studied with simulations in the future.

5. Summary

We analyzed an event of energy-dispersive field-aligned warm ion enhancements with increasing energy that is opposite from the dispersion seen in previously reported events. Based on our analysis presented here, we propose that the enhancements were a result of increasing outflow H^+ ions driven by enhanced convection and that it is the gradual increase of outflow ion energy accelerated by intensifying field-aligned potential that caused the dispersion signature with increasing energy. We used two THEMIS probes at $r \sim 7$ and 9 R_E around 01 hr MLT to investigate the temporal-spatial variations of energy-dispersive enhancements of field-aligned warm ions in the plasma sheet. Both probes observed similar energy-dispersion enhancements increasing energy from ~20 eV up to several hundreds of eV on a time scale of ~10 min, but the probe at smaller r observed the dispersive enhancement about 20 min later. The enhancements occurred during the growth phase of a small non-storm time substorm and the enhancements lasted until the probes observed dipolarization and BBFs. During the event, the radar and ground magnetometer observations in the vicinity of the probes' ionospheric footprints show that convection was enhanced and moved equatorward and that FACs were enhanced. Thus, enhanced Poynting flux associated enhanced convection likely drove more outflow ions into the plasma sheet. Also, DMSP passing through the auroral zone at ~01 hr MLT observed upward FACs with an associated upward field-aligned potential of ~100 eV. Thus, a gradual increase in the intensities of FACs and the associated upward field-aligned potential likely gradually increased the energy of the outflow ions from ~20 eV to above 100 eV, resulting in the observed energy-dispersive enhancement with increasing energy. In addition, the earthward penetration of convection, FACs, and field-aligned potential likely caused the enhancements seen first by TH-D at larger r and then later by TH-E at smaller r.

Data Availability Statement

The THEMIS data are available for free on the THEMIS website (http://themis.ssl.berkeley.edu/index.shtml). The solar wind and IMF parameters are available for free on NASA CDAWeb (http://cdaweb.gsfc.nasa.gov/cdaweb/istp_public/). The AE and SYM-H indices from Word Data Center for Geomagnetism, Kyoto are available for free on NASA CDAWeb (http://cdaweb.gsfc.nasa.gov/cdaweb/istp_public/). The Geotail data are available for free on the DARTS website (http://www.darts.isas.jaxa.jp/stp/ geotail/data.html). The SuperDARN data are available for free on the Virginia Tech SuperDARN website (http://vt.superdarn.org/tiki-index.php). The SuperMAG data are available for free on the SuperMAG website (https://supermag.jhuapl.edu/). The DMSP data are available for free on the SSUSI website (https://ssusi.jhuapl.edu/) for aurora images, on CEDAR Madrigal Database (http://cedar.openmadrigal.org/) for magnetic fields and precipitation fluxes, and on NASA CDAWeb (http://cdaweb.gsfc.nasa.gov/cdaweb/istp_public/) for plasma flow velocities.

Acknowledgments
C.-P. Wang is supported by NASA 80NSSC22K1012 and NSF-GEM 2224108. Xueyi Wang and Yu Lin are supported by NASA 80NSSC22K1012 and NSF-GEM 2224109. Simon Wing is supported by NASA Grants 80NSSC20K0704 and 80NSSC22K0515. We thank Vassilis Angelopoulos for THEMIS data. We thank K.H. Glassmeier, U. Auster, and W. Baumjohann for THEMIS/FGM data, C.W. Carlson and J. P. McFadden for the THEMIS/ESA data. We thank J. H. King, N. Papatashvilli at AdnetSystems, NASA Goddard Space Flight Center and CDAWeb for providing the OMNI data. We acknowledge Word Data Center for Geomagnetism, Kyoto for providing the AE and SYM-H indices. We thank DARTS for providing Geotail/MFM data. The authors acknowledge the use of SuperDARN data. SuperDARN is a collection of radars funded by national scientific funding agencies of Australia, Canada, China, France, Italy, Japan, Norway, South Africa, United Kingdom and the United States of America. We thank Prof M. J. Kosch of SANSA for permission to use SuperDARN South Africa data which was supported from a grant from SANAP (South African National Antarctic Program). The authors acknowledge the use of the on-line ray tracing tool hosted by the Virginia Tech SuperDARN group at their website. We thank SuperMAG for providing data from two British Antarctic Survey (BAS) magnetometers and BAS PI Mervyn Freeman for advice. We thank DMSP SSUSI team and Yongliang Zhang for SSUSI aurora image.

References

Angelopoulos, V. (2008). The THEMIS mission. *Space Science Reviews*, *141*(1–4), 5–34. https://doi.org/10.1007/s11214-008-9336-1

Auster, H. U., Glassmeier, K. H., Magnes, W., Aydogar, O., Baumjohann, W., Constantinescu, D., et al. (2008). The THEMIS fluxgate magnetometer. *Space Science Reviews*, *141*(1–4), 235–264. https://doi.org/10.1007/s11214-008-9365-9

Borovsky, J. E., Denton, M. H., Denton, R. E., Jordanova, V. K., & Krall, J. (2013). Estimating the effects of ionospheric plasma on solar wind/magnetosphere coupling via mass loading of dayside reconnection: Ion-plasma-sheet oxygen, plasmaspheric drainage plumes, and the plasma cloak. *Journal of Geophysical Research: Space Physics*, *118*(9), 5695–5719. https://doi.org/10.1002/jgra.50527

Chappell, C. R., Huddleston, M. M., Moore, T. E., Giles, B. L., & Delcourt, D. C. (2008). Observations of the warm plasma cloak and an explanation of its formation in the magnetosphere. *Journal of Geophysical Research*, *113*(A9), A09206. https://doi.org/10.1029/2007JA012945

Chaston, C. C., Bonnell, J. W., Wygant, J. R., Kletzing, C. A., Reeves, G. D., Gerrard, A., et al. (2015). Extreme ionospheric ion energization and electron heating in Alfvén waves in the storm time inner magnetosphere. *Geophysical Research Letters*, *42*(24), 10531–10540. https://doi.org/10.1002/2015GL066674

Davis, T. N., & Sugiura, M. (1966). Auroral electrojet activity index AE and its universal time variations. *Journal of Geophysical Research*, *71*(3), 785–801. https://doi.org/10.1029/JZ071i003p00785

Giles, B. L., Chappell, C. R., Moore, T. E., Comfort, R. H., & Waite, J. H., Jr. (1994). Statistical survey of pitch angle distributions in core (0–50 eV) ions from Dynamics Explorer 1: Outflow in the auroral zone, polar cap, and cusp. *Journal of Geophysical Research*, *99*(17), 483. https://doi.org/10.1029/94JA00864

Gjerloev, J. W. (2012). The SuperMAG data processing technique. *Journal of Geophysical Research*, *117*(A9), A09213. https://doi.org/10.1029/2012JA017683

Gkioulidou, M., Ohtani, S., Ukhorskiy, A. Y., Mitchell, D. G., Takahashi, K., Spence, H. E., et al. (2019). Low-energy (<keV) O+ ion outflow directly into the inner magnetosphere: Van Allen Probes observations. *Journal of Geophysical Research: Space Physics*, *124*(1), 405–419. https://doi.org/10.1029/2018JA025862

Gkioulidou, M., Wang, C.-P., Lyons, L. R., & Wolf, R. A. (2009). Formation of the Harang reversal and its dependence on plasma sheet conditions: Rice convection model simulations. *Journal of Geophysical Research*, *114*(A7), A07204. https://doi.org/10.1029/2008JA013955

Hardy, D. A., Schmitt, L. K., Gussenhoven, M. S., Marshall, F. J., Yeh, H. C., Shumaker, T. L., et al. (1984). Precipitating electron and ion detectors (SSJ/4) for the block 5D/flights 6–10 DMSP satellites: Calibration and data presentation. *Rep. AFGL-TR-84-0317, Bedford, Mass: Air Force Geophysics*. Laboratory Hanscom Air Force Base.

Heelis, R. A., & Hanson, W. B. (1998). Measurements of thermal ion drift velocity and temperature using planar sensors. In R. F. Pfaff, J. E. Borovsky, & D. T. Young (Eds.), *Measurement techniques in Space plasmas: Particles, geophysical monograph series* (Vol. 102, pp. 61–71). American Geophysical Union.

Horwitz, J. L., & Chappell, C. R. (1979). Observations of warm plasma in the dayside plasma trough at geosynchronous orbit. *Journal of Geophysical Research*, *84*(A12), 7075. https://doi.org/10.1029/JA084iA12p07075

Hull, A. J., Agapitov, O., Mozer, F. S., McFadden, J. P., & Angelopoulos, V. (2021). A survey of dense low energy ions in Earth's outer magnetosphere: Relation to solar wind dynamic pressure, IMF, and magnetospheric activity. *Journal of Geophysical Research: Space Physics*, *126*(9), e2021JA029208. https://doi.org/10.1029/2021JA029208

Hull, A. J., Chaston, C. C., Bonnell, J. W., Wygant, J. R., Kletzing, C. A., Reeves, G. D., & Gerrard, A. (2019). Dispersive Alfvén wave control of O+ ion outflow and energy densities in the inner magnetosphere. *Geophysical Research Letters*, *46*(15), 8597–8606. https://doi.org/10.1029/2019GL083808

Kistler, L. M., Mouikis, C. G., Spence, H. E., Menz, A. M., Skoug, R. M., Funsten, H. O., et al. (2016). The source of O^+ in the storm time ring current. *Journal of Geophysical Research: Space Physics*, *121*(6), 5333–5349. https://doi.org/10.1002/2015JA022204

Kokubun, S., Yamamoto, T., Acuña, M. H., Hayashi, K., Shiokawa, K., & Kawano, H. (1994). The GEOTAIL magnetic field experiment. *Journal of Geomagnetism and Geoelectricity*, *46*(1), 7–21. https://doi.org/10.5636/jgg.46.7

Lyatskaya, S., Lyatsky, W., & Zesta, E. (2016). Effect of interhemispheric currents on equivalent ionospheric currents in two hemispheres: Simulation results. *Journal of Geophysical Research: Space Physics*, *121*(2), 1339–1348. https://doi.org/10.1002/2015JA021167

Maggiolo, R. (2015). Auroral arcs and ion outflow. In Y. Zhang & L. J. Paxton (Eds.), *Auroral dynamics and Space weather*. https://doi.org/10.1002/9781118978719.ch4

McFadden, J. P., Carlson, C. W., Larson, D., Ludlam, M., Abiad, R., Elliott, B., et al. (2008). The THEMIS ESA plasma instrument and in-flight calibration. *Space Science Reviews*, *141*(1–4), 277–302. https://doi.org/10.1007/s11214-008-9440-2

Meng, C.-I., & Kroehl, H. (1977). Intense uniform precipitation of low-energy electrons over the polar cap. *Journal of Geophysical Research*, *82*(16), 2305–2313. https://doi.org/10.1029/JA082i016p02305

Merayo, J. M. G., Jørgensen, J. L., Friis-Christensen, E., Brauer, P., Primdahl, F., Jørgensen, P. S., et al. (2008). *Small satellites for Earth observation* (pp. 143–151). Springer.

Nagai, T., Johnson, J. F. E., & Chappell, C. R. (1983). Low-energy (less than 100 eV) ion pitch angle distributions in the magnetosphere by ISEE 1. *Journal of Geophysical Research*, *88*(A9), 6944. https://doi.org/10.1029/JA088iA09p06944

Nishida, A. (1994). The GEOTAIL mission. *Geophysical Research Letters*, *21*(25), 2871–2873. https://doi.org/10.1029/94GL01223

Nosé, M., Keika, K., Kletzing, C. A., Spence, H. E., Smith, C. W., MacDowall, R. J., et al. (2016). Van Allen Probes observations of magnetic field dipolarization and its associated O+ flux variations in the inner magnetosphere at L < 6.6. *Journal of Geophysical Research: Space Physics*, *121*(8), 7572–7589. https://doi.org/10.1002/2016JA022549

Nosé, M., Matsuoka, A., Miyoshi, Y., Asamura, K., Hori, T., Teramoto, M., et al. (2021). Field-aligned low-energy O+ flux enhancements in the inner magnetosphere observed by Arase. *Journal of Geophysical Research: Space Physics*, *126*(8), e2021JA029168. https://doi.org/10.1029/2021JA029168

Paxton, L. J., Schaefer, R. K., Zhang, Y., Kil, H., & Hicks, J. E. (2018). SSUSI and SSUSI-lite: Providing space situational awareness and support for over 25 years. *Johns Hopkins APL Technical Digest*, *34*(3).

Peterson, W. K., Andersson, L., Callahan, B. C., Collin, H. L., Scudder, J. D., & Yau, A. W. (2008). Solar-minimum quiet time ion energization and outflow in dynamic boundary related coordinates. *Journal of Geophysical Research*, *113*(A7), A07222. https://doi.org/10.1029/2008JA013059

Rich, F. J. (1984). *Fluxgate magnetometer (SSM) for the Defense meteorological satellite Program (DMSP) block 5D-2, flight 7. Tech. Rep. AFGL-TR-84-0225, air force geophys*. Lab., Hanscom Air Force Base.

Rich, F. J. (1994). *Users guide for the topside ionospheric plasma monitor (SSIES, SSIES-2, and SSIES-3) on spacecraft of the Defense meteorological satellite Program (DMSP). Volume I*. Technical Description, Phillips Laboratory Technical Report PL-TR-94-2187.

Strangeway, R. J., Ergun, R. E., Su, Y.-J., Carlson, C. W., & Elphic, R. C. (2005). Factors controlling ionospheric outflows as observed at intermediate altitudes. *Journal of Geophysical Research*, *110*(A3), A03221. https://doi.org/10.1029/2004JA010829

Tsyganenko, N. A. (1995). Modeling the Earth's magnetospheric magnetic field confined within a realistic magnetopause. *Journal of Geophysical Research*, *100*(A4), 5599–5612. https://doi.org/10.1029/94ja03193

Tsyganenko, N. A. (1996). Effects of the solar wind conditions on the global magnetospheric configuration as deduced from data-based field models. *Proceedings of the ICS-3 conference on substorms*. (Vol. 389, pp. 181–185). European Space Agency.

Wang, C.-P., Gkioulidou, M., Lyons, L. R., Wolf, R. A., Angelopoulos, V., Nagai, T., et al. (2011). Spatial distributions of ions and electrons from the plasma sheet to the inner magnetosphere: Comparisons between THEMIS-Geotail statistical results and the Rice convection model. *Journal of Geophysical Research*, *116*(A11), A11216. https://doi.org/10.1029/2011JA016809

Wing, S., Khazanov, G. V., Sibeck, D. G., & Zesta, E. (2019). Low energy precipitating electrons in the diffuse aurorae. *Geophysical Research Letters*, *46*(7), 3582–3589. https://doi.org/10.1029/2019GL082383

Wing, S., & Newell, P. T. (1998). Central plasma sheet ion properties as inferred from ionospheric observations. *Journal of Geophysical Research*, *103*(A4), 6785–6800. https://doi.org/10.1029/97JA02994

Yue, C., Wang, C.-P., Nishimura, Y., Murphy, K. R., Xing, X., Lyons, L., et al. (2015). Empirical modeling of 3-D force-balanced plasma and magnetic field structures during substorm growth phase. *Journal of Geophysical Research: Space Physics*, *120*(8), 6496–6513. https://doi.org/10.1002/2015JA021226